Fast ion confinement in the presence of core magnetic islands in Wendelstein 7-X

Samuel A. Lazerson[1], Joachim Geiger[1], David Kulla[1], Alexandra LeViness[2], Sergey Bozhenkov[1], Carsten Killer[1], Kunihiro Ogawa[3], Mitsutaka Isobe[3], Paul McNeely[1], Norbert Rust[1], Dirk Hartmann[1], and the W7-X Team

[1]Max-Planck-Institut fü Plasmaphysik, Wendelsteinstr. 1, Greifswald, Germany 17491

E-mail: samuel.lazerson@ipp.mpg.de

[2]Princeton Plasma Physics Laboratory, 100 Stellarator Rd., Princeton, USA 08540

[3]National Institute for Fusion Science, National Institutes of Natural Sciences, 322-6 Oroshi-cho, Toki, Japan

Abstract. The effect of magnetic islands in the core region of Wendelstein 7-X (W7-X) on fast ion confinement is explored through simulations with the BEAMS3D code. A magnetic configuration where the $n/m = 5/5$ island chain is shifted to $r/a \sim 0.7$ allows the exploration of core island physics in W7-X. The control coil system on W7-X allows the tuning of the island size either increasing the island width or decreasing it. A coupling of the BEAMS3D code to the FIELDLINES code provides a versatile mechanism for incorporating magnetic islands and stochastic regions into the BEAMS3D code. Collisionless simulations suggest that the presence of core islands degrade the confinement of passing particles in the region of the island chain. Full neutral beam simulations of W7-X show a similar behavior with confinement decreasing as the island width is increased. Comparisons between a vacuum magnetic field and low beta HINT2 simulation are made showing similar fast ion behavior. Measurements of lost fast ions in W7-X confirm this trend with the control coil suppressed island configuration showing lower losses than that with no control coils applied. Simulations of fast ion wall loads are performed suggesting no drastic change in loss pattern and a slight reduction in losses with minimized islands.

1. Introduction

In this work, fast ion confinement in the presence of magnetic islands is explored through simulations of Wendelstein 7-X (W7-X)[1]. Magnetic islands play a ubiquitous role in stellarators given their three dimensional nature [2]. Much effort has been spent in the design and construction of stellarators to minimize the presence of magnetic islands [3]. More recently the topic has been explored in the plasmas of the Large Helical device (LHD) and the TJ-II stellarator [4]. There the presence of plasma response (flows) can play a determining role in how (and whether) islands form in stellarators. The ability of the W7-X main coils to scan the $n/m = 5/5$ intrinsic island position, coupled with auxiliary coils designed to directly modify this island chain make W7-X an excellent place to study such physics [5, 6, 7, 8]. In particular, the role magnetic islands may play in energetic particle confinement can be studied. To this end, the BEAMS3D code [9] has been modified to include radial mapping of islands, allowing simulations of neutral beam injection (NBI) to be performed. This work provides a basis for assessment of fast ion confinement when magnetic islands are present in the confinement volume of W7-X.

The presence of magnetic islands in magnetically confined fusion devices is generally considered detrimental as they degrade confinement. A magnetic island arrises in such a device when a magnetic flux surface with rational rotational transform resonates with a magnetic field normal to the surface. The transform (ratio of poloidal to toroidal magnetic flux $\iota = d\Psi/d\Phi$) is considered rational when the orbit of the field lines in that surface can be described by an integer ratio of a poloidal to toroidal transits, for example $\iota = n/m = 1/2$ implying two poloidal turns per toroidal turn. When a radial field with equal mode structure is applied to such a flux surface, the orbits of those field lines in the flux surface bifurcate forming a field line trajectory known as a magnetic island. It should be noted that for a single pure perturbing field two periodic orbits in the unperturbed flux surface will remain: one which is stable and one which is unstable. The stable orbit is essentially unperturbed and is called the 'o-point'. Neighboring field lines, of the 'o-point', form nested surfaces around this point giving the magnetic island its characteristic shape. The unstable orbit is know as the 'x-point'. Neighboring field lines, of the 'x-point', bifurcate forming a separatrix around the island. The degradation in confinement comes from the volume filling nature of the island, allowing particles moving along, and across, the field line to quickly traverse a large radial region. This can result in a zero pressure gradient region of finite volume appearing in the plasma, reducing the overall stored energy. The situation becomes much worse as neighboring islands grow and form stochastic regions through overlap.

While the above explanation of island physics is correct in the vacuum limit, the presence of a plasma significantly modifies the picture. Pressure gradients in plasmas result in local currents which generate their own magnetic fields giving rise to new sources of resonant magnetic fields. While axisymmetric systems avoid the formation of resonant field with increasing plasma pressure, in stellarators resonant magnetic fields are formed giving rise to a form of beta-limit [10, 11]. Ion and electron orbits in the

vicinity of an island can experience different effects. This is attributed to the difference in their masses giving rise to different gyro radii, often experimentally seen through a flattening of the electron temperature but not ion temperature. Finally, the finite collisionality and local plasma flows can further influence what happens at an island. In LHD this effect is quite dramatic resulting in so-called 'healing' of externally induced magnetic islands due to neoclassical orbit effects [12, 13, 14].

The complex interplay between the three dimensionality of stellarator flux surfaces and vacuum magnetic fields makes the reduction of magnetic islands a key topic in stellarator optimization. To this end various techniques have been employed to reduce and suppress island formation in stellarators. The HELIAS line of stellarators, of which W7-X is a member, relies on low magnetic shear ($d\iota/d\rho$) to avoid low order rational surfaces all together (except at the edge where a large island chain forms a divertor). Additionally, the optimization of W7-X focused on minimizing the Shafranov shift along with bootstrap current, thus minimizing changes in the magnetic field as beta increases. This further helps to suppress islands. Devices such a NCSX and LHD have a high positive shear which helps limit the size to which an island could grow. Additionally, the coils of NCSX were re-optimized to minimize the formation of islands at finite plasma beta [3]. The ubiquitous nature of magnetic islands in stellarators has made their minimization a key factor in stellarator design.

Theoretical work motivated by experimental evidence from LHD and TJ-II suggests that the issue of magnetic islands in stellarator reactors may be overstated when the effect of the plasma is taken into account. In these devices, it was found that an $n/m = 1/1$ magnetic islands could 'heal' itself as plasma beta and collisionality was changed. In LHD, the magnetic island is induced by external perturbing coils and measured as flat-spots in the electron temperature profile and via a magnetic flux loop array [15]. This has been explained through the mechanism of neoclassical flows healing the magnetic islands. The phenomenology is similar to that of mode penetration in tokamaks as viewed in reverse, with flows growing to suppress islands as opposed to the tokamak situation where already present flows suppress the penetration of modes. In general, the data and theory suggest that at low collisionalities and high plasma betas, islands will heal. This implies that in stellarator reactors the issue of the formation of magnetic islands may be overstated, although they may still be present in the plasma initiation phase if care is not taken to avoid vacuum islands. Finally, evidence from LHD suggests that when islands are present there is not only a degradation in the thermal plasma confinement but a significant effect on the fast ion population [16].

While the nominal W7-X configurations were designed to avoid low order rationals in the confinement region, configurations with the $\iota = 1$ surface at mid radius are realizable. Such configurations are achieved by energizing the planar superconducting coils such that they produce a toroidal magnetic field and subsequently adjusting the non-planar superconducting coil currents to maintain the required on-axis magnetic field. In this work, the nonplanar coils were set to 13.6 kA and the planar coils to -5 kA creating the 'FOM' configuration [17]. The size of the intrinsic vacuum island
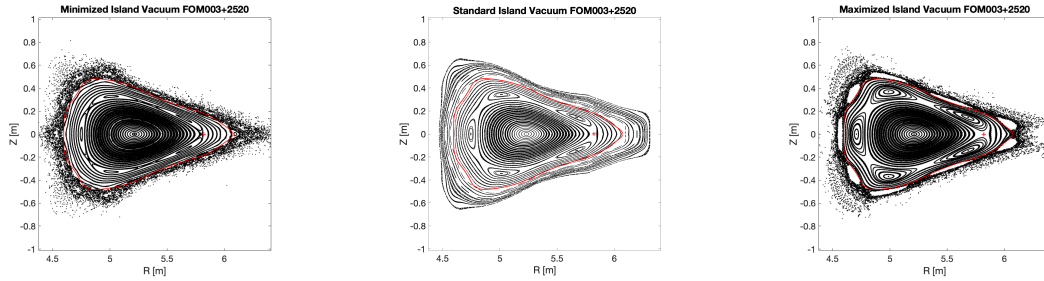
Figure 1. Vacuum Poincaré plots of the FOM W7-X magnetic configuration with control coil minimized (left), nominal (center), and maximized (right) $n/m = 5/5$ island chain.

chain ($n/m = 5/5$) can be modified by the 10 in-vessel island control coils. In figure 1, the island minimized, nominal and maximized configurations are visualized through Poincaré plots. Additionally, a $n/m = 1/1$ and $n/m = 2/2$ island structure may be superimposed via the trim coil system. In this work, focus is placed on the use of the control coils to control island width. In this way, similar studies to those performed in LHD can be undertaken.

One of the challenges to simulating fast ion confinement in this FOM configuration is mapping profile information in and around islands and stochastic regions. Traditionally, magnetic equilibrium (such as VMEC [18]) provide a mapping between flux surfaces and the background computation grid in codes such as BEAMS3D [9]. This is advantageous as the equilibrium pressure profile can be kept self consistent with the underlying kinetic profiles which are needed for neutral beam simulations (temperatures, densities, and electrostatic scalar potentials). Equilibrium codes, such as HINT [19], which include islands and stochastic regions cannot easily provide such a mapping for profile quantities (the same argument can be made for vacuum fields). Attempts have been made to construct such coordinates for the edge island region in W7-X, but such work is not well suited to a general purpose code such as BEAMS3D [20]. To this end a novel and robust technique based on field line following has been developed and interfaced to the BEAMS3D code. This allows the simulations of neutral beam injection using VMEC and HINT equilibria, along with vacuum fields.

In this work simulations of neutral beam generated fast ion confinement in the presence of magnetic islands is investigated for W7-X. In the next section we review our tools and methods for this investigation. In section 3 we present our simulation results for both collisionless particle orbits and full neutral beam simulations. In section 4, we place these results in the context of data so far collected on W7-X. Finally, in section 5 we provide an overview of our results and future research directions for this topic.

2. Method

The BEAMS3D code is used to model the effect of magnetic islands on neutral beam generated fast ions in W7-X. To achieve this the BEAMS3D code has been upgrade via an interface to the FIELDLINES code [21]. This interface provides BEAMS3D with both magnetic fields (from a variety of sources) and a radial gridding in regions with chaotic field line trajectories. Additionally, the FIELDLINES code itself was interfaced to the HINT code. This allows magnetic fields from MHD equilibria which contain magnetic islands and stochastic regions to be used in BEAMS3D. The 'FOM' W7-X magnetic configuration is modeled using VMEC (no islands), HINT (MHD equilibria with islands), and three vacuum configurations (reduced, nominal and large vacuum islands). Collisionless test particle simulations are preformed to understand how the magnetic islands affect specific orbits in W7-X. Full neutral beam simulations are performed to better assess the ability to measure the effect of islands on neutral beam generated fast ions.

2.1. Radial grids with islands and stochastic regions
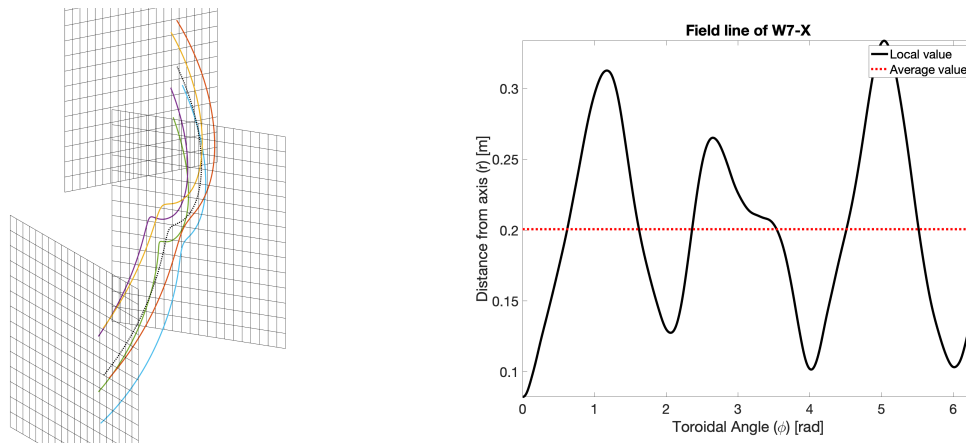
Figure 2. Schematic depiction of the field line trace (left) for grid formation and minor radius as a function of the field line trajectory (right). Magnetic axis is plotted in black for the field line trace, while colors indicate multiple passes for a single field line. We can clearly see that the local distance from the magnetic axis varies over the trajectory.

The generation of radial grids from general toroidal magnetic fields is performed using field line tracing. A background cylindrical grid, as found in both the BEAMS3D and FIELDLINES code, is assumed to exist on which the magnetic field is sampled. A similar gridding of the effective minor radius is sought. To achieve this, the magnetic axis in a symmetry plane is found using the pseudo-return map [22]. Once found, a set of field lines is traced with starting points stretching from the magnetic axis (R_{axis}, Z_{axis}) to the background grid maximum R extent (R_{grid}, Z_{axis}). The field lines are traced

for approximately 500 toroidal transits with values saved at each toroidal cut in the background grid. This essentially produces a Poincaré mapping at each toroidal cut of the background grid. The local distance between a given field line and the magnetic axis is then calculated for each point along the field line trajectory. This distance is then averaged along the field line and used to label the field line. At each point in the background grid the field lines passing near said grid point are identified. Here, near is defined as $\pm 0.5 \Delta R$ and $\pm 0.5 \Delta Z$ where ΔR is the distance between radial grid points and ΔZ is the distance between vertical grid points. The labels (being the average distance from the magnetic axis) are then averaged and this value stored at the evaluated grid point. In this way a radial grid can be generated from the magnetic field lines. A poloidal angle can be defined in a similar fashion. In figure 2, we depict this scheme in a schematic diagram and plot the value of the minor radius for a sample field line in the nominal vacuum magnetic field case for the 'FOM' magnetic configuration.

2.2. The FIELDLINES code

An algorithm for the generation of such a coordinate set has been implemented in the FIELDLINES code. The FIELDLINES code is designed to take a variety of magnetic field sources (coils[23], EQDSK equilibria [24], vacuum grid files, and VMEC equilibria [25]), place them on a cylindrical background grid, and solve the toroidal field line equations

$$\frac{dR}{d\phi} = R\frac{B_R}{B_\phi} = b_R \tag{1}$$

$$\frac{dZ}{d\phi} = R\frac{B_Z}{B_\phi} = b_Z. \tag{2}$$

where the cylindrical coordinates are (R, ϕ, Z) and the cylindrical components of the magnetic field are (B_R, B_ϕ, B_Z). It should be noted that this code is the predecessor of the BEAMS3D code, sharing much of its underlying structure.

In order to determine the magnetic axis, the FIELDLINES code makes use of the pseudo-return map. A slightly extended set of equations is followed for one transit in field periodicity,

$$\frac{dq_1}{d\phi} = b_R \tag{3}$$

$$\frac{dq_2}{d\phi} = b_Z \tag{4}$$

$$\frac{dq_3}{d\phi} = \frac{\partial b_R}{\partial R}q_3 + \frac{\partial b_R}{\partial Z}q_5 \tag{5}$$

$$\frac{dq_4}{d\phi} = \frac{\partial b_R}{\partial R}q_4 + \frac{\partial b_R}{\partial Z}q_6 \tag{6}$$

$$\frac{dq_5}{d\phi} = \frac{\partial b_Z}{\partial R}q_3 + \frac{\partial b_Z}{\partial Z}q_5 \tag{7}$$

$$\frac{dq_6}{d\phi} = \frac{\partial b_Z}{\partial R}q_4 + \frac{\partial b_Z}{\partial Z}q_6 \tag{8}$$

where the initial condition for $\vec{q} = (R_0, Z_0, 1, 0, 0, 1)$. We can easily see that the first two equations are simply the ODE for the field line trajectory. The other four integrals provide information on the pseudo-return map, which are then used to calculate an updated guess for the magnetic axis. This is written

$$R_1 = R_0 + \alpha\frac{\Delta q_6 \Delta q_1 - \Delta q_4 \Delta q_2}{\Delta q_3 \Delta q_6 - \Delta q_4 \Delta q_5} \tag{9}$$

$$Z_1 = Z_0 + \alpha\frac{\Delta q_5 \Delta q_1 + \Delta q_3 \Delta q_2}{\Delta q_3 \Delta q_6 - \Delta q_4 \Delta q_5} \tag{10}$$

where the initial position of the axis is (R_0, Z_0), the position after one full integration is (R_1, Z_1), Δq is the change in q over one field period, and α is a smoothing factor. It is essentially a Newton method and converges within a few iterations to machine precision. It should be noted that this method may be used for finding any 'periodic' field line orbit should the toroidal periodicity of the field line be known. In order to discriminate the magnetic axis the field line is only followed over one field period. In the absence of symmetry breaking error fields, only the magnetic axis will be found using this algorithm. It should be noted that when using an algorithm such as this for finding other periodic orbits, the pseudo-return map provides stability information allowing X- (unstable) and O-points (stable) to be discriminated. Additionally, for X-Points the map provide information for helping to trace the stable (separatrix) and unstable (homoclinic tangle) manifolds. In this work, only the axis finding aspect is utilized.

Once an axis is found, the code traces a set of field lines from the axis to the background grid outboard edge. Data is saved toroidally at each location in the cylindrical background grid. This mostly fills the space of the background grid with field line data. However, it is possible that the interior of an island may not be filled if its phase does not match the initial condition for the trace. To address this the code counts the number of field lines which pass near each grid point. Grid points where no field lines pass and neighboring grid points are then used to initialize field line traces. Doing this helps to fill the space sufficiently given a fixed background grid resolution. Figure 3 depicts the radial grid for the five cases considered in this work. In such simulations we have normalized the radial grid to a value of $0.66\ m$. We note that for the VMEC case, the traditional method of inverse lookup mapping with extrapolation outside the VMEC simulation domain was utilized. The extrapolation treats the even modes as linear in toroidal flux while the odd modes are treated as linear in r/a.

In order to extend the utility of the FIELDLINES and BEAMS3D codes, an interface was developed to the HINT2 code. HINT2 is a three dimensional equilibrium code employing islands and stochastic regions with a background cylindrical grid. Magnetic field information is stored on this background grid making the interfacing of such fields a trivial matter. However, no explicit radial grid exists in HINT2 with pressure and current stored on the background grid as well. Initial attempts to use
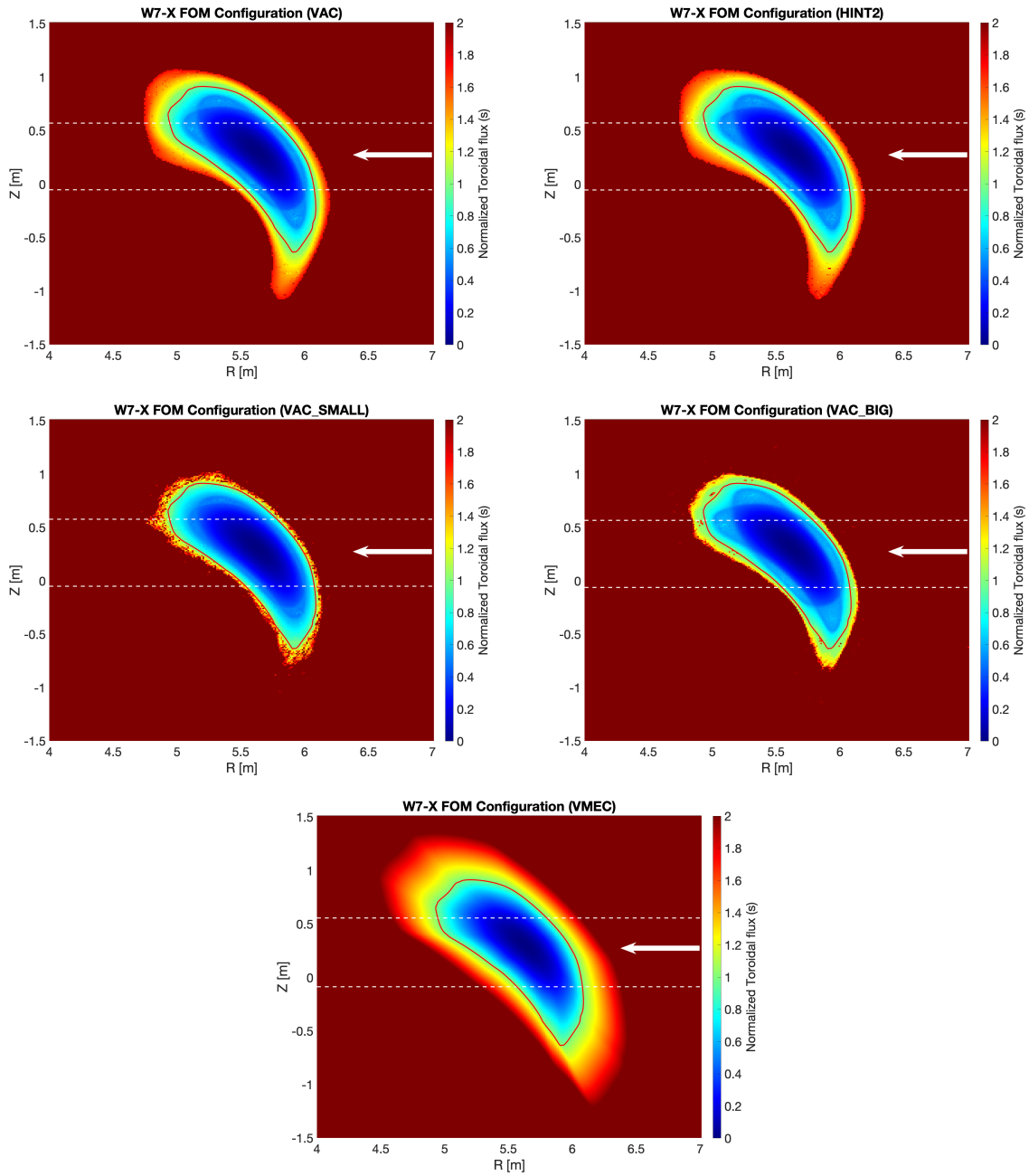
Figure 3. Radial coordinate mapping in the toroidal plane of the NI21 neutral beam box for the five cases considered here. A red isocontour has been added at the $r/a = 1$ surface in each plot. Dashed white lines indicate the vertical extent of neutral beam injection and direction of beam injection is indicated with a white arrow.

the pressure as a radial quantity made interpretation of results difficult. This method would require that the radial grid as a function of pressure be known. Development of the above method of coordinate construction was found to be a better choice (and extendable to other equilibrium codes as well).

2.3. The BEAMS3D code

The BEAMS3D code is a Monte-Carlo neutral beam injection Fokker-Planck code capable of treating three dimensional equilibria and three-dimensional walls. The code calculates neutral beam injection for W7-X using a beamlet model for the sources, full port model for beam scraping, and Suzuki model for hydrogen isotope beam deposition [26]. This aspect of the code has been validated against data from both W7-X and ASDEX-U [27, 28, 29]. The code stores data on a cylindrical background grid and pushes both gyro center and full orbit particles with slowing down and pitch angle scattering operators. Efforts to validate these models continue with various aspects of the fast ion distribution function being tested. The code also models the loss of fast ions to a fully three-dimensional wall [30]. In this way the BEAMS3D code provides a complete package for modeling neutral beam injected fast ions in stellarators and tokamaks with 3D fields.

In this work, the BEAMS3D code has been interfaced to the FIELDLINES code to provide interfaces to magnetic fields (both vacuum and equilibrium) which contain islands and stochastic regions. As the magnetic fields of the FIELDLINES code are also on a cylindrical grid, the BEAMS3D simulation simply inherits the background grid resolution of the FIELDLINES code. In this case $R = [4, 7]$ m, $Z = [-1.5, 1.5]$ m, and $\phi = [0, 2\pi/5]$ rad, with $nr = 256$, $nz = 256$, and $n\phi = 72$ grid points. Generation of the radial background grid is performed as was described in section 2.1 for the three vacuum cases and HINT case considered here. The VMEC case uses the previously documented interfaces. It is worthwhile to note that the presence of islands and stochastic regions does result in two curious features.

First, when trying to construct radial fast ion profiles of various quantities, the flat-spots in the rho coordinate result in a binning of a larger volumetric region of particles. Thus local enhancements of the profile appear despite the volumetric density profile being fairly smooth. Care must be taken when interpreting fast ion data in terms of 1D profiles.

Second, the BEAMS3D code includes an electric field by taking local gradients of the scalar potential stored on the background grid. This potential is defined as a flux function on input, resulting in an electric field feature near the separatrix of the magnetic island chain. The electric field used as input is based on neoclassical simulations assuming nested flux surfaces (VMEC).

Markers are pushed either using a gyro center model or gyro orbit model. The initial condition of the markers can either be user supplied or generated from the neutral beam injection model. When neutral beam injection is used, markers are initialized at the gyro-center position based on the ionization location of the neutral. For gyro orbit models the neutral ionization location is used. The equations of motion for the gyro center model are:

$$\frac{d\vec{R}}{dt} = \frac{\hat{b}}{qB} \times \left(\mu \nabla B + \frac{mv_\parallel^2}{B}(\hat{b} \cdot \nabla)\vec{B} \right) + v_\parallel \hat{b} + \frac{\vec{E} \times \vec{B}}{B^2}$$

$$\frac{dv_\parallel}{dt} = -\frac{\mu}{m}\hat{b}\cdot(\nabla B)$$

where $\hat{b} = \frac{\vec{B}}{B}$, $\mu = \frac{1}{2}\frac{mv_\perp^2}{B}$ is the magnetic moment, $\vec{E} = -\nabla\Phi$ is the electric field, and $v_\parallel = \frac{d\vec{R}}{dt}\cdot\hat{b}(\vec{R})$ is the component of velocity parallel to $\vec{B}$. It should be noted that a term in the second equation is missing, which accounts for electric fields parallel to the magnetic field. This term is explicitly missing as we assume only 'radial' electric fields. Whereas the gyro orbit model equation are written

$$\frac{d\vec{R}}{dt} = \vec{v}$$

$$\frac{d\vec{v}}{dt} = \frac{q}{m}\left(\vec{E} + \vec{v}\times\vec{B}\right)$$

where the Lorentz force is the right hand side of the second equation. The gyro center model is applied to simulations up to a user specified value of normalized toroidal flux ($s = \sqrt{r/a}$ where a a minor radius), after which full orbit simulations are carried out. Setting this parameter to zero triggers the code to use the full orbit model from birth (or user supplied initial condition).

In this work, fully collisional neutral beam simulations are performed in addition to collisionless simulations with user specified initial conditions. Collisional slowing down operators and pitch angle scattering are considered in the neutral beam simulations.

2.4. The W7-X simulations

The simulations performed in this work focus on five magnetic field scenarios: no islands (VMEC), minimized islands (vacuum), nominal islands (vacuum), nominal islands (HINT2), and maximized islands (vacuum). For neutral beam simulations, profiles are chosen to approximate those of experiments conducted in W7-X. Figure 4 depicts the kinetic profiles assumed in each simulation. The choice of one set of profiles was made to clearly highlight that any differences between configurations is attributed to the magnetic field itself and not some temperature or density effect. The electrostatic scalar potential is based on neoclassical calculations using VMEC equilibria. It should be noted that while common radial kinetic profiles are utilized, changes due to the islands result in different profiles locally. This is addressed in the neutral beam deposition simulations.

For this work the neutral beam sources 4 in neutral beam box NI20 and 7 in neutral beam box NI21 are considered. The NI20 box geometry results in particles with $\left|v_\parallel/v\right| < 0$, while the NI21 box geometry results in particles with $\left|v_\parallel/v\right| > 0$ [31]. This choice of sources was name to allow later comparison with measurements made during the last experimental campaign. It should be noted that source 4 generates a larger passing population than source 7. This is attributed to the crossing of source beam lines through the duct, with NBI sources 4 and 8 firing more tangentially, and sources 3 and 7 firing more radially. The use of both boxes allows the NI20 box to produce a sources of fast ions while the NI21 box is used to probe that population through measurements of FIDA [32, 33].
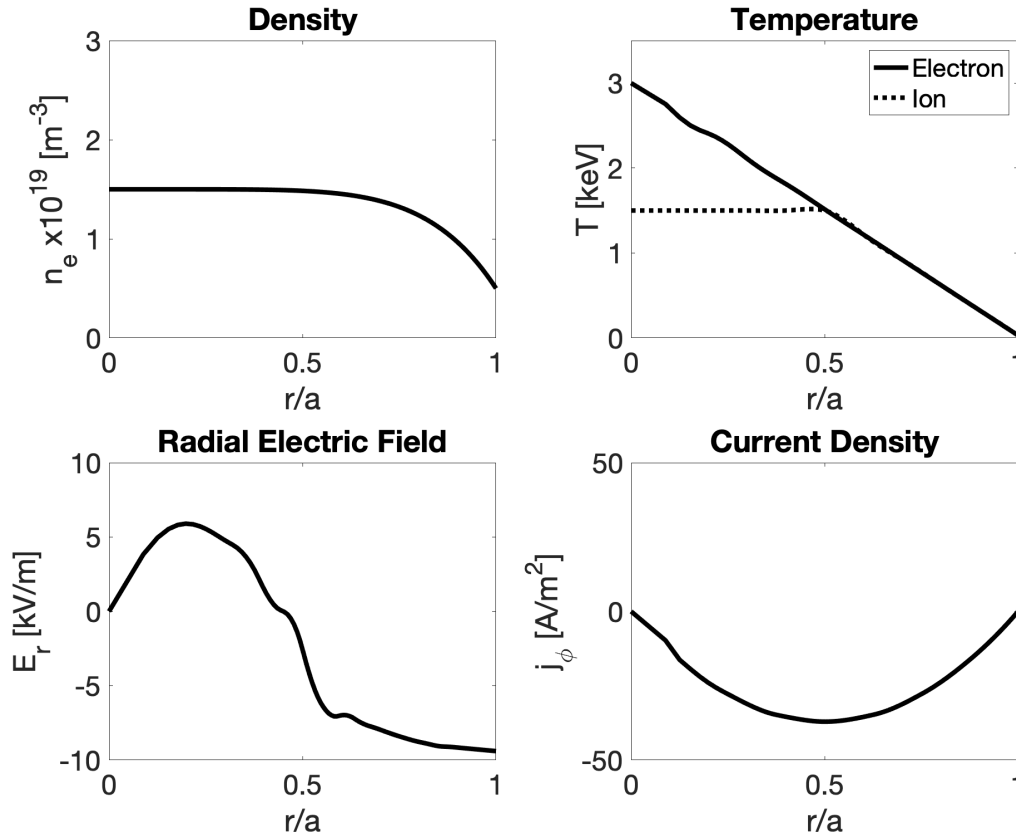
Figure 4. Kinetic profiles for all simulations performed in this work. A pure $Z_{effective} = 1$ plasma is assumed. Electric field profile and total toroidal current from NEOTRANSP. Simple current profile shape is assumed.

3. Results

In this work, both collisionless test particle simulations and neutral beam simulations were considered. In the collisionless simulations an array of markers were initialized just inside the 5/5 island surface, scanning pitch angle. These particles are followed in the absence of collisions to better assess how the presence of magnetic islands affects different orbits. In the neutral beam simulations, collisional deposition, gyro-center slowing down and full orbit simulations are performed. The full orbit simulations begin when the orbits cross the $r/a = 1.0$ radial coordinate.

3.1. Collisionless orbit tracing

Collisionless simulations following test particles scanning pitch angle in the W7-X FOM configuration are performed. All simulations tracked particle scanning pitch angle from the co- to counter-going direction. Simulations scanning the initial location of test particles showed that for any effect to be seen the particles must be started in the

vicinity of the island chain. Moreover, little difference was seen if the particles where started in the vicinity of the x-point or o-point. Comparisons between gyro center and gyro orbit following models also showed little difference. This is to be expected as the 2.5 T field of W7-X results in an order $\sim 2\ cm$ gyroradius.
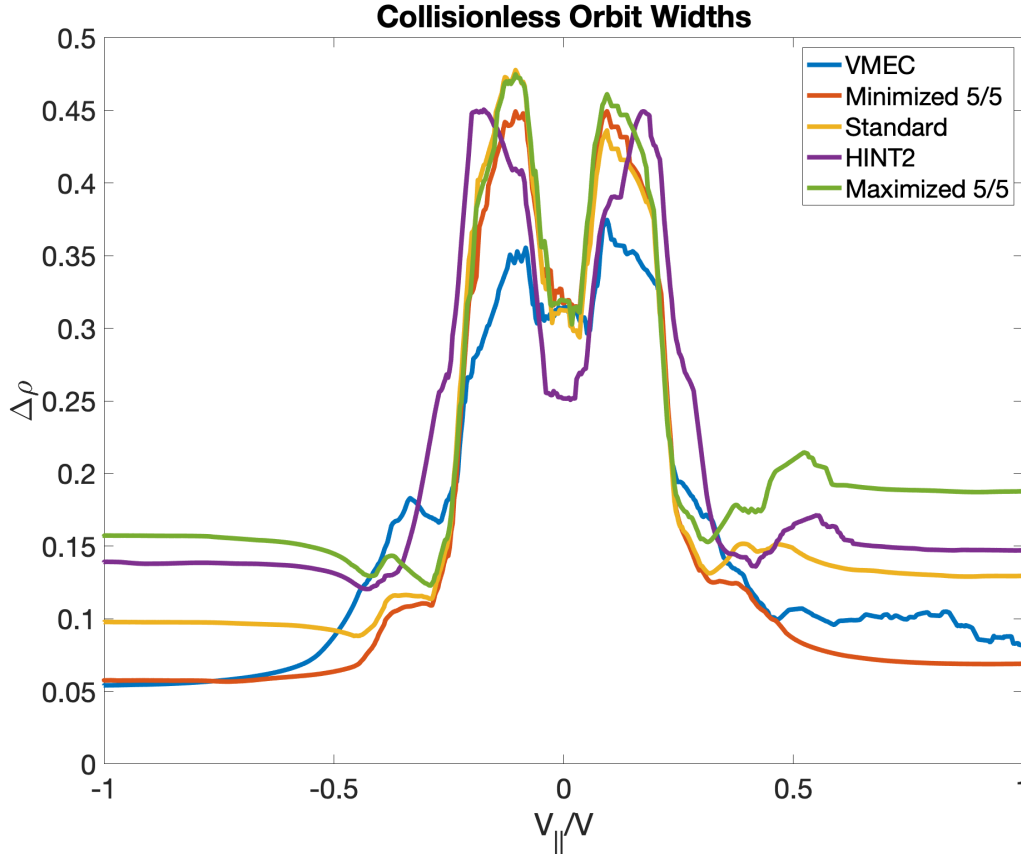
Figure 5. Orbit widths for an ensemble of collisionless particle orbits. Orbit widths are calculated from the difference between minimum and maximum values of normalized toroidal flux reached in a simulation. Widths greater than 0.25 can be considered lost particles. A smoothing has been applied to the curves to make the plots more readable.

Figure 5 shows the orbit widths for the particles based on their minimum and maximum radial positions. These simulations indicate that the passing particle orbit widths scale with the vacuum island width. All deeply trapped particles walk radially outward till they are lost. It is interesting to note that in all cases the particles parallel to the magnetic field ($v_{\parallel}/v > 0$) appear to have a slightly larger orbit widths than those counter to the magnetic field. Examining the maximum and minimum parallel velocities we see that particles begin to trap when $\left|v_{\parallel}/v\right| < 0.4$. Examining the toroidal motion of the particles we find that deeply trapped particles, particles which do no leave their initial toroidal well, are limited to $\left|v_{\parallel}/v\right| < 0.18$. This just highlights the complexity of orbits in W7-X where trapping can occur due to both toroidal and poloidal variation of magnetic fields in the device.

Confinement of deeply trapped particles in W7-X is expected to improve with beta through the closing of drift surfaces and the $\vec{E} \times \vec{B}$ drift resulting in a poloidal precession of deeply trapped particles. A scan of the electric field strength was made to estimate its effect on the particle orbits. In general, passing orbits were found to have larger radial excursions in the presence of a radial electric field. The deeply trapped particles experienced a smaller radial drift as compared to a simulation without the radial electric field. It should be noted that since BEAMS3D prescribes the electrostatic scalar potential (Φ_{es}) as a radial flux function, the island influences the electric field ($\vec{E} = -\nabla \Phi_{es}$). In particular, strong electric fields arise at the island separatrix in the model.
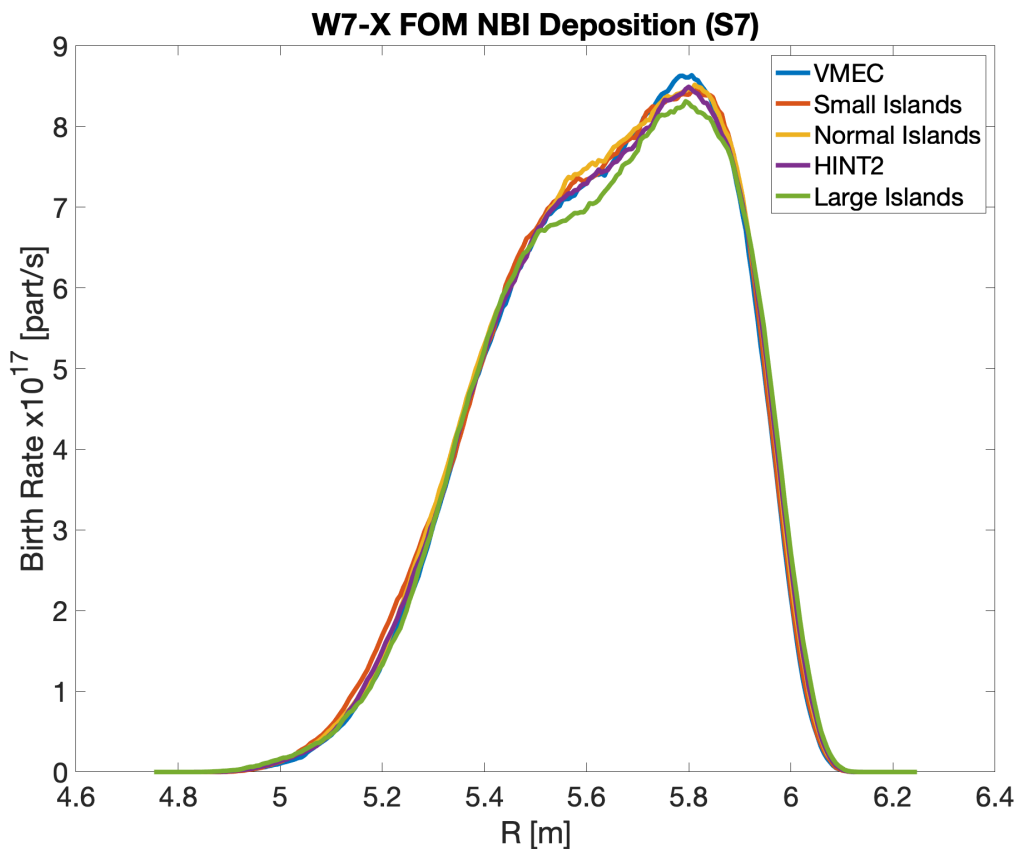
Figure 6. Fast ion birth rates for source 7 of the five magnetic fields considered in this work showing little difference between configurations.

3.2. Neutral beam simulations

Simulations of neutral beam injection have been performed in three steps for the five different magnetic field variations (vacuum small island, vacuum nominal island, vacuum large island, VMEC, HINT2). In each simulation the experimental profiles are held fixed. Only the magnetic field, and underlying topology, change the mapping of the profiles

to real space. Simulations begin with neutral beam deposition considering a detailed port model. Particles which ionize in the plasma are then stepped to the gyrocenter position and followed untill all particles have been lost or thermalized. For the VMEC case a wall is autogenerated at the last closed flux surface (LCFS) by the BEAMS3D code. For the other cases the VMEC boundary is expanded by 10% and used as a wall. Particles which hit these walls are considered lost. Finally, these lost particles are followed in gyro-orbit mode to the actual W7-X wall including the full magnetic field. In this last step collisions and the electric field are ignored, owing to the large uncertainty in specifying such quantities outside the LCFS. For this work sources NBI 4 and 7 are considered. Table 1 provides an overview of simulation global quantities.

Table 1. Overview of neutral beam simulations for the various magnetic field variations. Simulations assume injection via NBI sources 4 and 7, 3600 MW total neutralized power. In each case, 380 kW is lost to the neutral beam port, and 2100 kW of power is lost as shine-through.

| Magnetic Field Source	Plasma Heating [kW]	Wall Losses [kW]
VMEC	960	160
Small Vacuum Islands	1020	100
Nominal Vacuum Islands	1020	100
HINT2	920	200
Large Vacuum Islands	980	140

The neutral beam simulations begin with simulations of neutral beam deposition including a detailed port model and experimentally relevant profiles. The simulations assume a neutralized power of 1.8 MW for a total of 3.6MW. Before entering the torus 380 kW of power is lost to the various port structures. While small variations in shine-through exist between the simulations, they can be all characterized as having 2100 kW of total shine-though. Such high shine-through is consistent with the low plasma density of these scenarios. Figure 6 depicts little variation between configurations regarding the deposition profiles.

Figure 7 depicts the birth profile mapped to rho coordinate showing a clear spike at the $\iota = 1$ surface. This feature is geometrical in nature and not a physical effect. Such distributions are generated by mapping flux marker locations in cylindrical space to radial grid space using the background grid. The presence of an island creates regions of constant radial coordinate which then map multiple points to a single point in the radial coordinate space. Plotting the distribution against the rotational transform shows that such a spike localizes to the $\iota = 1$ surface. A plot of the differential volume is shown in order to demonstrate that such a feature does not arise from our volume normalization. Additionally, we see that the location of the spike in rho scales with the island width as one would expect since the island moves slightly radially outward with increasing size. It can also been seen that the nominal vacuum island simulations produces a similar profile
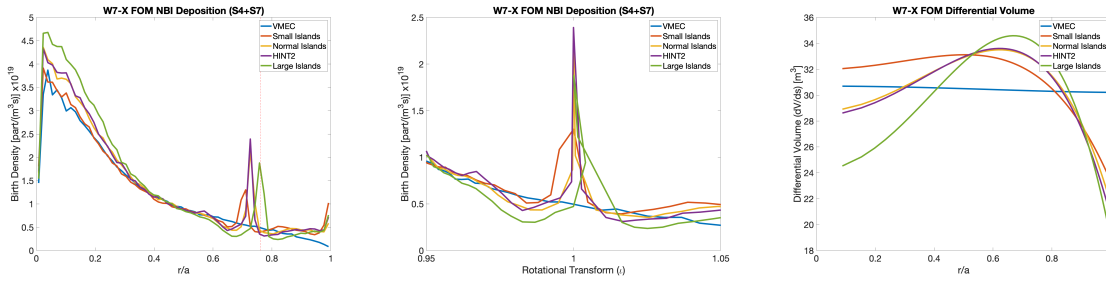
Figure 7. Fast ion birth profile mapped to rho (left), rotational transform (center), and differential volume (right) showing that spikes are localized to the $\iota = 1$ surface. A dashed red line has been drawn at the VMEC $iota = 1$ radial grid point.

to that of the HINT2 simulation as they have very similar magnetic island structure.
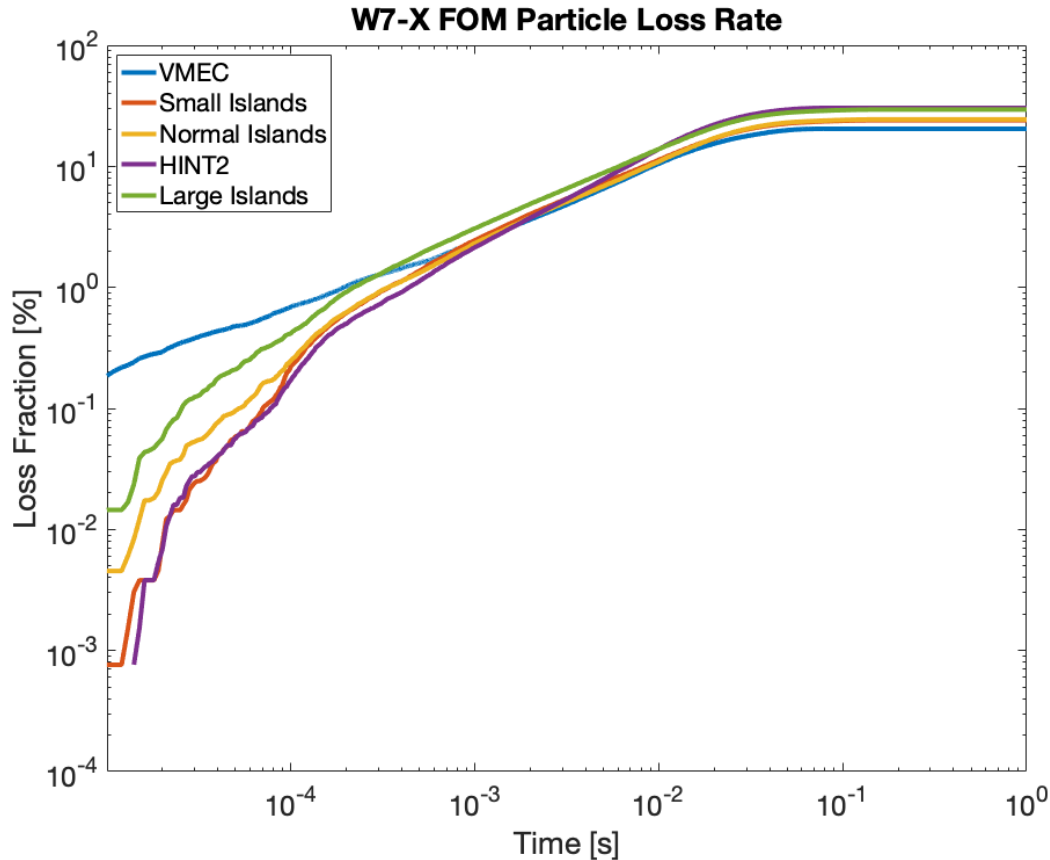
Figure 8. Marker losses for the five simulations considered showing VMEC with the lowest marker loss and HINT2 with the highest for gyrocenter simulations.

Gyro center slowing down simulations including pitch angle scattering were performed for the five sources of magnetic field. Markers were initialized from the neutral beam deposition simulations. Figure 8 depicts the time evolution of the marker loss. On

full slowing down time scales we find the HINT2 simulation to have the largest losses while VMEC has the lowest. On timescales less that $0.1ms$ we find just the opposite with VMEC having the most prompt losses and HINT2 the least. On short timescales we find the vacuum islands have a scaling consistent with our collisionless simulations picture with the small island case having the lowest losses. As time progresses the nominal and small islands cases have similar losses both in energy and particle loss. This suggests that for those cases the losses induced by pitch angle scattering dominate the simulations.


Figure 9. Fast ion wall loads for a synthetic view from the fast ion wall load monitor diagnostic. The HINT2 simulations results are shown.

The gyro center simulations were then continued to the first wall of W7-X using the gyro orbit capability of the BEAMS3D code [30]. Gyro center markers which reached a bounding flux surface were used as an initial condition for the gyro orbit simulations. These markers were duplicated 4 times each and the duplicated particles were assigned random gyro phases. A small difference in wall loads is present with the small island case having the lowest losses. Figure 9 shows a simulated view from the Fast Ion Wall Load Monitor camera to be installed for the next experimental campaign on W7-X. A clear load is present on the divertor viewing immersion tube in the AEF port. NBI

fast ion losses to these immersion tubes are a well established feature of many magnetic configurations in W7-X [34, 35]. Of key interest is the lower heat load on the steel panel. Simulations would suggest this load would be enough to damage the panels at our current NBI duration. Despite this, no damage has been found or evidence that the panel is getting hot. The current hypothesis is that the neglect of a scrape-off-layer, edge electric field, and charge exchange losses of fast ions results in our current over prediction of some fast ion wall loads.

4. Experimental Data
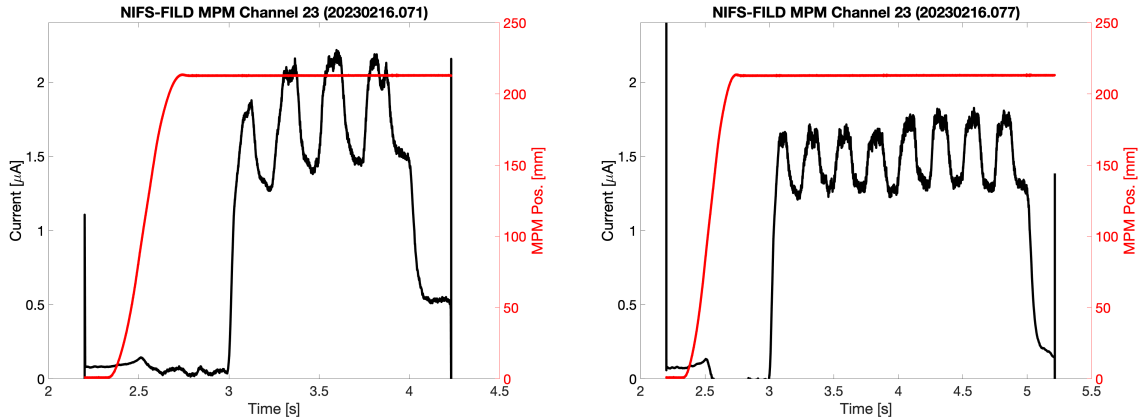
Figure 10. NIFS-FILD signal for the FOM magnetic configuration with nominal 5/5 islands (left) and control coil minimized islands (right). The overall signal level is decreased for the minimized island configuration, consistent with simulations. The neutral beam is active from 3 s on in both discharges, with source 4 continuous and source 7 blipped at 4 Hz and 50% duty cycle.

Experiments in this core island magnetic configuration have thus far been limited in the W7-X dataset. Figure 10 shows traces of a single channel on the NIFS-FILD detector for two discharges [36]. In these discharges source 4 is fired continuously while source 7 is blipped at 4 Hz and 50% duty cycle. In the figure on the left (20230216.071) no trim or control coil currents were applied to the plasma. On the right (20230216.077), the control coils were energized with -2500 A of current, minimizing the island width. Losses from the S7 source are clearly reduced when the island width is minimized. Additionally, the baseline signal from source 4 appears to also slightly reduce in magnitude. This is consistent with expectations as source 7 populates purely passing orbits, while source 4 populates the multiply trapped orbits. For this reason one would expect island size variation to have a larger effect on the source 7 population. In each discharge 2 MW of ECRH heating was applied with a target line integrated density of $2 \times 10^{19}\ m^{-2}$. Core electron temperatures were approximately 3 keV and the line integrated density rises to $3 \times 10^{19}\ m^{-2}$ during neutral beam injection. Simulations of signals to the NIFS-FILD detector are subject of ongoing work [37], along with FIDASIM simulations [38].

5. Discussion

Simulations of fast ion confinement in the presence of core magnetic islands have been performed using the BEAMS3D code for Wendelstein 7-X. A newly developed interface based on field line tracing using the FIELDLINES code has been implemented allowing construction of radial grids in islands and stochastic regions. Such an interface is general and allowed for both interfacing vacuum magnetic fields in addition to HINT2 equilibria. A magnetic configuration with the $n/m = 5/5$ island chain at $r/a \sim 0.7$ was explored. Application of control coil fields allows control of the vacuum island width. Collisionless test particle simulations show that confinement of passing particles is directly affected by the island, with larger islands degrading confinement. Simulations with VMEC equilibria had a similar character to those with the vacuum island minimized, while HINT2 calculations showed similar behavior to that of the nominal vacuum island configuration. Neutral beam deposition showed little response to the magnetic island width. Slowing down simulations showed a degradation in confinement with increasing island width. Loss patterns to the first wall were generally unaffected by changes in island width while the amplitude of the losses tracked the degradation in confinement. Experiments conducted in the previous experimental campaign confirm this behavior with a reduced island configuration showing smaller losses. Such simulations open the possibility to assessing fast ion confinement using equilibria from a variety of equilibrium codes, capable of treating islands and stochastic regions.

With the understanding that the W7-X neutral beam system populates the passing orbits, whose confinement is affected by the presence of core islands, NBI fast ion confinement can be used as a probe for the existence of islands at finite beta. While an effect on fast ion confinement was clearly seen for low beta discharges, at higher plasma beta islands may undergo healing. In devices such as LHD, this is commonly confirmed by the lack of a flat electron temperature region across the rational surface. Unfortunately, the Thomson system in W7-X shoots thought the X-points of the 5/5 island chain, and as a result would not see a significant change in electron temperature as an island healed or opened. Here changes in fast ion confinement could be used as an indicator of island width changes. One could also use a combination of the control coils and trim coils to minimize the 5/5 island chain while introducing a large $n/m = 1/1$ or $n/m = 2/2$ island chain (figure 11). Such experiments would provide a comparison to, and extension of, work already conducted on LHD.

Acknowledgments
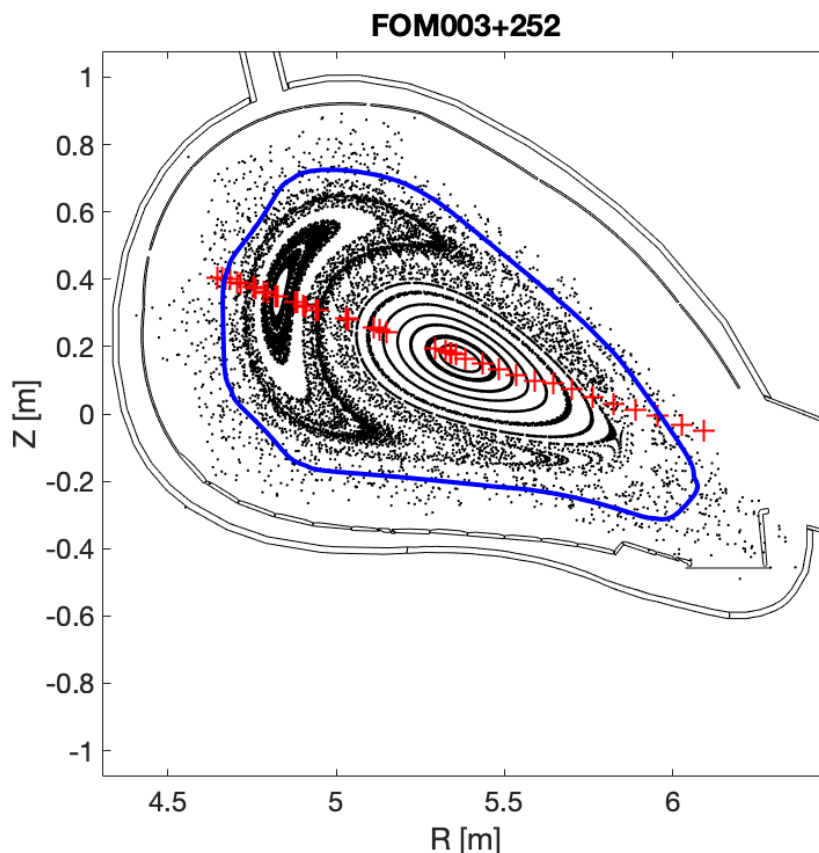
Figure 11. Poincaré plot of the FOM magnetic configuration with suppressed $n/m = 5/5$ island chain and large trim coil induced $n/m = 1/1$ vacuum island. Red crosses indicate approximate Thomson scattering volumes, while the solid blue line depicts the configuration's last closed flux surface.

Commission can be held responsible for them.

References

[1] Wolf R C, Alonso A, Äkäslompolo S, Baldzuhn J, Beurskens M, Beidler C D, Biedermann C, Bosch H S, Bozhenkov S, Brakel R, Braune H, Brezinsek S, Brunner K J, Damm H, Dinklage A, Drewelow P, Effenberg F, Feng Y, Ford O, Fuchert G, Gao Y, Geiger J, Grulke O, Harder N, Hartmann D, Helander P, Heinemann B, Hirsch M, Höfel U, Hopf C, Ida K, Isobe M, Jakubowski M W, Kazakov Y O, Killer C, Klinger T, Knauer J, König R, Krychowiak M, Langenberg A, Laqua H P, Lazerson S, McNeely P, Marsen S, Marushchenko N, Nocentini R, Ogawa K, Orozco G, Osakabe M, Otte M, Pablant N, Pasch E, Pavone A, Porkolab M, Puig Sitjes A, Rahbarnia K, Riedl R, Rust N, Scott E, Schilling J, Schroeder R, Stange T, von Stechow A, Strumberger E, Sunn Pedersen T, Svensson J, Thomson H, Turkin Y, Vano L, Wauters T, Wurden G, Yoshinuma M, Zanini M, Zhang D and the Wendelstein 7-X Team 2019 *Physics of Plasmas* **26** 082504 ISSN 1070-664X, 1089-7674 URL http://aip.scitation.org/doi/10.1063/1.5098761

[2] Nührenberg C, Boozer A H and Hudson S R 2009 *Physical Review Letters* **102** 235001 ISSN 0031-9007, 1079-7114 URL https://link.aps.org/doi/10.1103/PhysRevLett.102.235001

[3] Hudson S R, Monticello D A and Reiman A H 2001 *Phys. Plasmas* **8** 5

[4] Narushima Y, Castejón F, Sakakibara S, Watanabe K, Ohdachi S, Suzuki Y, Estrada T, Medina F, López-Bruna D, Yokoyama M, Yoshinuma M, Ida K, Nishimura S, LHD Experiment Group and TJ-II Experiment Group 2011 *Nuclear Fusion* **51** 083030 ISSN 0029-5515, 1741-4326 URL https://iopscience.iop.org/article/10.1088/0029-5515/51/8/083030

[5] Andreeva T, Kisslinger J and Wobig H 2002 *Issues of atomic science and technology* ISSN 1562-6016 national Scientific Center Kharkiv Physical and Technical Institute NAS of Ukraine URL http://dspace.nbuv.gov.ua/xmlui/handle/123456789/80261

[6] Andreeva T, Geiger J, Dinklage A, Wurden G, Thomsen H, Rahbarnia K, Schmitt J C, Hirsch M, Fuchert G, Nührenberg C, Alonso A, Beidler C D, Beurskens M N A, Bozhenkov S, Brakel R, Brandt C, Bykov V, Grahl M, Grulke O, Killer C, Kocsis G, Klinger T, Krämer-Flecken A, Lazerson S, Otte M, Pablant N, Schilling J, Windisch T and Team t W X 2022 *Nuclear Fusion* **62** 026032 ISSN 0029-5515 publisher: IOP Publishing URL https://dx.doi.org/10.1088/1741-4326/ac3f1b

[7] Rummel T, Risse K, Kisslinger J, Koppen M, Fullenbach F, Neilson H, Brown T and Ramakrishnan S 2012 *IEEE Transactions on Applied Superconductivity* **22** 4201704–4201704 ISSN 1051-8223, 1558-2515 URL http://ieeexplore.ieee.org/document/6117068/

[8] Fullenbach F, Risse K, Rummel T, Eeten P V, Carls A, Volzke O, Haas M and Bosch H S 2020 *IEEE Transactions on Plasma Science* 1–4 ISSN 0093-3813, 1939-9375 URL https://ieeexplore.ieee.org/document/8994199/

[9] McMillan M and Lazerson S A 2014 *Plasma Physics and Controlled Fusion* **56** 095019

[10] Suzuki Y, Watanabe K Y and Sakakibara S 2020 *Physics of Plasmas* **27** 102502 ISSN 1070-664X URL https://doi.org/10.1063/5.0015106

[11] Loizu J, Hudson S R and Nührenberg C 2016 *Physics of Plasmas* **23** 112505 ISSN 1070-664X, 1089-7674 URL http://aip.scitation.org/doi/10.1063/1.4967709

[12] Hegna C 2011 *Nuclear Fusion* **51** 113017 ISSN 0029-5515, 1741-4326 URL https://iopscience.iop.org/article/10.1088/0029-5515/51/11/113017

[13] Hegna C C 2011 *Plasma Physics and Controlled Fusion* **53** 024003 ISSN 0741-3335, 1361-6587 URL https://iopscience.iop.org/article/10.1088/0741-3335/53/2/024003

[14] Hegna C C 2012 *Physics of Plasmas* **19** 056101 ISSN 1070-664X URL https://doi.org/10.1063/1.3694042

[15] Narushima Y, Sakakibara S, Suzuki Y, Watanabe K, Ohdachi S, Takemura Y, Yoshinuma M, Ida K, Castejón F, López-Bruna D, Hegna C, Kobayashi M, Tanaka H, Akiyama T, Ohno N and The LHD Experiment Group 2017 *Nuclear Fusion* **57** 076024 ISSN 0029-5515, 1741-4326 URL https://iopscience.iop.org/article/10.1088/1741-4326/aa6dce

[16] Yamaguchi H and Murakami S 2016 *Plasma and Fusion Research* **11** 2403094 ISSN 1880-6821 URL https://www.jstage.jst.go.jp/article/pfr/11/0/11_2403094/_article

[17] Laqua H P 2022 Nomenclature for magnetic configurations at w7-x Tech. Rep. 28YVHR Max-Planck-Institut für Plasmaphysik https://idm.ipp-hgw.mpg.de/?uid=28YVHR

[18] Hirshman S P and Whitson J C 1983 *Physics of Fluids* **26** 3553–3568

[19] Suzuki Y, Nakajima N, Watanabe K, Nakamura Y and Hayashi T 2006 *Nuclear Fusion* **46** L19–L24 ISSN 0029-5515, 1741-4326 URL https://iopscience.iop.org/article/10.1088/0029-5515/46/11/L01

[20] Schmitt J C, Kriete D M, Andreeva T, Geiger J, Grahl M, Schilling J, Thomsen H and Flom E 2022 *Plasma Physics and Controlled Fusion* **64** 055022 ISSN 0741-3335 publisher: IOP Publishing URL https://dx.doi.org/10.1088/1361-6587/ac5f3f

[21] Engels D, Lazerson S A, Bykov V and Proll J H E 2022 *Plasma Physics and Controlled Fusion* **64** 035003 ISSN 0741-3335, 1361-6587 URL https://iopscience.iop.org/article/10.1088/1361-6587/ac43ef

[22] Meiss J D 1992 *Reviews of Modern Physics* **64** 795–848 publisher: American Physical Society URL https://link.aps.org/doi/10.1103/RevModPhys.64.795

[23] Hanson J D and Hirshman S P 2002 *Physics of Plasmas* **9** 4410–4412 ISSN 1070-664X, 1089-7674

URL `http://aip.scitation.org/doi/10.1063/1.1507589`

[24] Lao L L, John H S, Stambaugh R D, Kellman A G and Pfeiffer W 1985 *Nuclear Fusion* **25** 1611 ISSN 0029-5515 URL `https://dx.doi.org/10.1088/0029-5515/25/11/007`

[25] Hirshman S P and Whitson J 1983 *Physics of Fluids* **26** 3553 ISSN 00319171 URL `https://aip.scitation.org/doi/10.1063/1.864116`

[26] Suzuki S, Shirai T, Nemoto M, Tobita K, Kubo H, Sugie T, Sakasai A and Kusama Y 1998 *Plasma Physics and Controlled Fusion* **40** 2097–2111 ISSN 0741-3335, 1361-6587 URL `https://iopscience.iop.org/article/10.1088/0741-3335/40/12/009`

[27] Lazerson S A, Ford O P, Nuehrenberg C, Äkäslompolo S, Poloskei P Z, Machielsen M, McNeely P, Vanó L, Rust N, Bozhenkov S, Neelis T W, Graves J P, Pfefferlé D, Spanier A, Hartmann D, Marushchenko N, Turkin Y, Hirsch M, Chaudhary N, Hoefel U, Stange T, Weir G, Pablant N, Langenberg A, Traverso P, Valson P, Knauer J, Jakob Brunner K, Pasch E, Beurskens M, Damm H, Fuchert G, Nelde P, Scott E, Hergenhahn U, Pavone A, Rahbarnia K, Andreeva T, Schilling J, Brandt C, Neuner U, Thomsen H, Jakubowski M, Ali A, Gao Y, Niemann H, Puig Sitjes A, Koenig R, Wolf R C and W7-X 2020 *Nuclear Fusion* **60** 076020 ISSN 0029-5515, 1741-4326 URL `https://iopscience.iop.org/article/10.1088/1741-4326/ab8e61`

[28] Kulla D 2023 Validation of the BEAMS3D slowing down model using fidasim on asdex upgrade in preparation

[29] Lazerson S A, Pfefferlé D, Drevlak M, Smith H, Geiger J, Äkäslompolo S, Xanthopoulos P, Dinklage A, Ford O, McNeely P, Rust N, Bozhenkov S, Hartmann D, Rahbarnia K, Andreeva T, Schilling J, Brandt C, Neuner U, Thomsen H, Wolf R C and W7-X Team T 2021 *Nuclear Fusion* **61** 096005 ISSN 0029-5515, 1741-4326 URL `https://iopscience.iop.org/article/10.1088/1741-4326/ac0771`

[30] Lazerson S A, Kulla D, Hartmann D A, McNeely P, Rust N and Team t W X 2023 *Nuclear Fusion* **63** 096012 ISSN 0029-5515 publisher: IOP Publishing URL `https://dx.doi.org/10.1088/1741-4326/ace9ec`

[31] Rust N, Heinemann B, Mendelevitch B, Peacock A and Smirnow M 2011 *Fusion Engineering and Design* **86** 728–731 ISSN 09203796 URL `https://linkinghub.elsevier.com/retrieve/pii/S0920379611003279`

[32] Mencke J E, Moseev D, Salewski M, Larsen M R, Schmidt B S, Järleblad H, Lazerson S, Poloskei P Z and Ford O 2022 *Review of Scientific Instruments* **93** 123503 ISSN 0034-6748 publisher: American Institute of Physics URL `https://aip.scitation.org/doi/10.1063/5.0128594`

[33] Poloskei P Z, Geiger B, Jansen van Vuuren A, Akaslompolo S, Ford O P, Spanier A, Neelis T, McNeely P and Hartmann D 2023 *Nuclear Fusion* ISSN 0029-5515 URL `http://iopscience.iop.org/article/10.1088/1741-4326/ad0dd4`

[34] Cornelissen M J H, Lazerson S A, Gao Y, Proll J H E, McNeely P, Rust N, Hartmann D, Jakubowski M W, Ali A, Pisano F, Niemann H, Sitjes A P, König R, Wolf R C and Team t W X 2022 *Plasma Physics and Controlled Fusion* **64** 125015 ISSN 0741-3335 publisher: IOP Publishing URL `https://dx.doi.org/10.1088/1361-6587/aca0bf`

[35] Äkäslompolo S, Drewelow P, Gao Y, Ali A, Bozhenkov S, Fellinger J, Geiger J, Hartmann D, Hathiramani D, Jakubowski M, McNeely P, Mohr S, Niemann H, Pisano F, Rust N, Puig Sitjes A, Sleczka M and Wolf R 2019 *Fusion Engineering and Design* **146** 862–865 ISSN 09203796 URL `https://linkinghub.elsevier.com/retrieve/pii/S0920379619301127`

[36] Ogawa K, Bozhenkov S, Äkäslompolo S, Killer C, Grulke O, Nicolai D, Satheeswaran G, Isobe M, Osakabe M, Yokoyama M and Wolf R 2019 *Journal of Instrumentation* **14** C09021–C09021 ISSN 1748-0221 URL `https://iopscience.iop.org/article/10.1088/1748-0221/14/09/C09021`

[37] LeViness A, Lazerson S, Jansen van Vuuren A, Rueda-Rueda J, Bozhenkov S, Garcia-Munoz M, Killer C, Ogawa K, Pablant N *et al.* 2023 Development of synthetic diagnostics for fast ion loss detection systems in wendelstein 7-x *49th EPS Conference on Plasma Physics*

[38] Kulla D Modeling wendelstein 7-x plasmas with fidasim and beams3d